Measurement 121 (2018) 127–138

Contents lists available at ScienceDirect

Measurement

journal homepage: www.elsevier.com/locate/measurement

Reconstruction of extreme topography from UAV structure from motion photogrammetry

Francisco Agüera-Vega[a,*], Fernando Carvajal-Ramírez[a], Patricio Martínez-Carricondo[a], Julián Sánchez-Hermosilla López[a], Francisco Javier Mesas-Carrascosa[b], Alfonso García-Ferrer[b], Fernando Juan Pérez-Porras[b]

[a] Dept. of Engineering, Univ. of Almeria, Campus de Excelencia Internacional Agroalimentario, ceiA3, Spain
[b] Dept. of Graphic Engineering and Geomatics, Campus de Rabanales, University of Cordoba, Córdoba 14071, Spain

ARTICLE INFO

Keywords:
Unmanned aerial vehicle (UAV)
UAV photogrammetry
Structure from motion (SfM)
Cut slope
Extreme topography
Landslide

ABSTRACT

The development of unmanned aerial vehicle photogrammetry over the last decade has allowed terrain that is very difficult for humans to access to be captured at very high spatial and temporal resolutions. This paper deals with the application of this technique to the study of extreme topography in a near-vertical road cut-slope. Three photogrammetric projects were carried out: one derived from images taken with the camera oriented horizontally, one derived from images taken with the camera tilted at 45°, and one derived from both sets of images. Point clouds and orthophotos were generated for each of these projects. The best accuracies were achieved by the photogrammetric products derived from the combined images set, which had RMSE equal to 0.053 m, 0.070 m and 0.061 m in X, Y and Z direction, respectively. A software program was developed to generate contour lines and cross-sections derived from the point cloud, which was able to represent all terrain geometric characteristics, such as several Z coordinates for a given planimetric (X, Y) point. Furthermore, comparing the contour lines and cross-sections generated from the point cloud using the program developed in this project to those generated from the digital surface model showed that the former are capable of representing geometric terrain characteristics that the latter cannot.

1. Introduction

During the past decade there have been rapid technological developments related to digital elevation modelling. For most of geomorphic applications, topographic surveys have been largely conducted using robotic total stations [1] or differential global navigation satellite systems (GNSS) [2,3]. Nowadays, new technologies, such as terrestrial laser scanning (TLS) [4], aerial laser scanning (ALS) [5,6], and softcopy photogrammetry [7], have improved the accuracy of digital elevation models (DEMs), but they are often time-consuming and costly.

Landforms with complex topography can render these methodologies unusable and even prove dangerous for operators. Furthermore, in the most dynamic environments it is necessary to employ a high temporal frequency of data collection at a very high spatial resolution in order to study their evolution. This is especially necessary when landform evolution may cause both human and economic disaster, as in the case of infrastructure built on these kinds of landforms.

In order to overcome the limitations of traditional techniques, the use of consumer grade cameras mounted on unmanned aerial vehicles (UAVs) to recover terrain information has been the subject of investigation for the past several years [8,9]. UAVs present distinct advantages over conventional piloted aircrafts and satellites, particularly their low cost, operational flexibility, and better spatial and temporal resolution [10,11,12,13]. UAVs require less time than other techniques for data acquisition and, therefore, reduce costs [14]. Moreover, UAV imagery provides results at a resolution and accuracy that cannot currently be met by satellite-derived products [15] and which are very useful in places where the use of other techniques is dangerous. The rapid development of these systems in recent years, and the miniaturization of sensors, have increased the civil applications of UAVs [16]. A detailed description of this evolution and the state of the art can be found in [17], and a review of the applications of UAVs in civil engineering, in general, and in 3D mapping application, in particular, can be found in [18] and [19], respectively.

The integration of computer vision and image analysis has resulted in a technique called structure-from-motion (SfM) [20], which

* Corresponding author.
E-mail addresses: faguera@ual.es (F. Agüera-Vega), carvajal@ual.es (F. Carvajal-Ramírez), pmc824@ual.es (P. Martínez-Carricondo), jusanche@ual.es (J. Sánchez-Hermosilla López), fjmesas@uco.es (F.J. Mesas-Carrascosa), ir1gapoa@uco.es (A. García-Ferrer), 012ppof@uco.es (F.J. Pérez-Porras).

https://doi.org/10.1016/j.measurement.2018.02.062
Received 8 January 2018; Received in revised form 21 February 2018; Accepted 26 February 2018
Available online 27 February 2018

automatically solves for the geometry of the scene and the camera positions and orientations without the need to specify a priori a network of targets which have known 3D positions [21,22,23]. SfM incorporates multi-view stereopsis (MSV) techniques [24,25], which derives 3D structure from overlapping photography acquired from multiples angles. Lowe [26], Snavely et al. [21], and Forsman et al. [27], applied a scale-invariant feature transform (SIFT) operator for key-point detection for generating 3D point clouds from photographs. Some researchers have concluded that this operator is one of the most robust for large image variations [28,29] [28,29]. SfM with MVS has surpassed the low precision shown by traditional photogrammetric DEMs when compared to airborne LiDAR, as demonstrated by authors who obtained terrain models with centimeter precision and point cloud resolutions that fell between airborne LiDAR and TLS [30]. A more detailed description of SfM can be found in [3,23].

Recent studies have been carried out using UAV imagery and SfM techniques for geomorphologic and terrain mapping purposes. Harwin and Lucieer [11] report accuracies of 0.025–0.040 m in the point cloud of a natural landform generated from UAV imagery and SfM techniques. Lucieer et al. [31] generated a high-resolution Digital Surface Model (DSM) of Antarctic moss beds from UAV imagery obtaining an overall root mean square error (RMSE) of 0.420 m. Mancini et al. [32] studied the creation and validation of point clouds and DSM generated from images of a beach dune system taken by a digital single-lens reflex (DSLR) camera mounted on a rotatory-wing UAV. The UAV-based approach was demonstrated to be straightforward, and the accuracy of the vertical dataset was comparable with results obtained by TLS technology. Lucieer et al. [33] used UAV imagery for mapping landslide displacements. Their DEMs and orthoimages were exported at a resolution of 1 cm resulting in a $RMSE_{XY}$ of 0.070 m and a $RMSE_Z$ of 0.062 m. Tonkin et al. [34] used a rotary-wing UAV to recover images for topographic surveys and they concluded that the DSM produced from the UAV imagery was in good agreement with the total station survey points. Eltner et al. [35] measured surface changes of short-term erosion events using images taken from a rotary-wing UAV; these data were compared to a DSM produced with TLS data, showing that DSMs have an accuracy of less than one centimeter. Mozas-Calvache et al. [36] yielded a methodology based on UAV photogrammetry techniques to study landslide evolution. In their study of a landslide affecting an urban zone, Mateos et al. [37] used techniques combining satellite and UAV images to accurately detect land displacements rates over time.

The work of Clapuyt et al. [9] compared different SfM-derived topography datasets resulting from identical replications and observed, in all cases, measurements precisions on the order of centimeters, demonstrating the reproducibility of UAV-based Earth topography reconstructions based on SfM algorithms.

In [38,39] the influence of several factors (flight altitude, number and of ground control points (GCPs), and terrain morphology) on DSM and orthoimages obtained with UAV photogrammetry, was explored. With a flight altitude of 50 m and 10 GCP, the researches obtained accuracies of 0.053 m in planimetry and 0.049 m in altimetry, but all of the morphologies studied allowed access to any point to take coordinate measurements or perform other related works. Fernández et al. [40] conducted an analysis of landslide evolution by studying the terrain displacements over several years. The terrain morphology and the objective of this work required adapting the usual UAV photogrammetry methodology, using GCPs which were static throughout the duration of the study which was in a complex terrain morphology. Carvajal-Ramírez et al. [41] studied a very complex landslide morphology with inaccessible areas. They only used GCPs located around the study area and compared the accuracies of photogrammetric projects with different images orientations: images oriented orthogonal to the terrain, and classical vertical image orientation. They concluded that the orthogonal image methodology is more appropriate for this kind of morphology.

In summary, there have been great development in UAV photogrammetry in recent years, and it is increasingly used in situations where classical photogrammetry is less efficient or simply not applicable. All of this makes it necessary to continue the development of specific methodologies to obtain accurate results using UAV photogrammetry in extreme situations when classical photogrammetry is not applicable.

This paper provides a methodology to obtain photogrammetrically-derived topographic information from UAV imagery of extreme and dynamic topography, where traditional techniques are dangerous or impossible to apply. Our goals were to quantify the accuracy of the generated point cloud and produce cartographic information for terrains with extreme morphology that is useful for engineers, geologists, and other technicians. In this way, the results obtained in the present work, besides providing knowledge about the geometric accuracy of UAV photogrammetry, will constitute a working methodology that will be useful in civil engineering works that would otherwise be more expensive or impossible to carry out.

2. Study area

The study area covers a cut slope located on the N-340 road, in the province of Almería, southeast Spain, between Almería city and Aguadulce (Fig. 1). The SW and NE rectangle vertices covering the studied area are 540117, 4074712, and 540453, 4074967, respectively (UTM coordinates Zone 30N, European Terrestrial Reference System 1989: ETRS89).

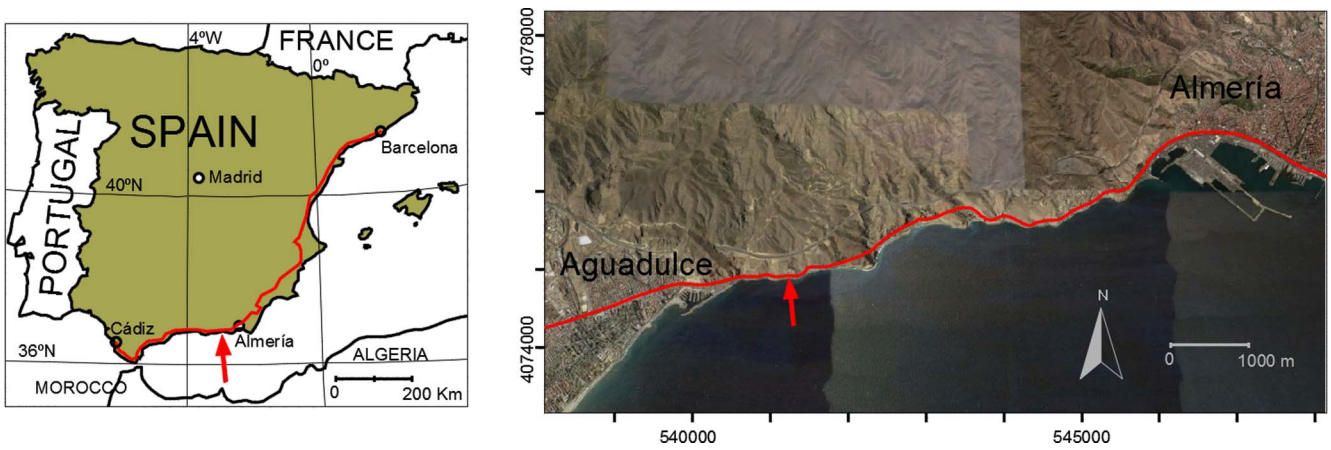

Fig. 1. Geographical location of the study area. The red arrow indicates the location of the study area. The red line represents the N-340 road. (For interpretation of the references to colour in this figure legend, the reader is referred to the web version of this article.)

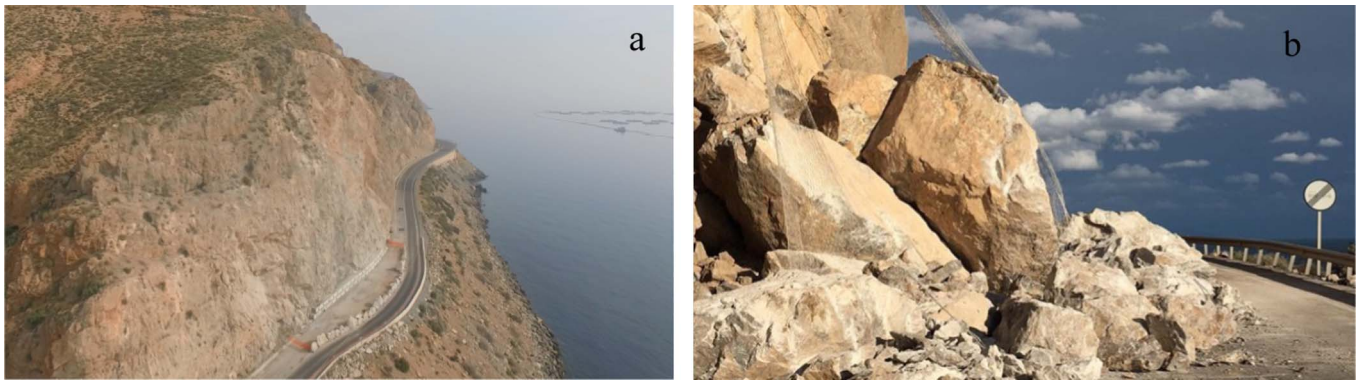

Fig. 2. Studied cut-slope (a) and landslide caused by torrential rains (b).

The studied cut slope is 130 m long and the greatest elevation difference between the road and the top of the cut-slope is 70 m (Fig. 2a). It has almost vertical slopes and even some areas with negative slopes, i.e., overhangs where part of the cut-slope is suspended over the road. Furthermore, it suffered a landslide caused by torrential rains (Fig. 2b) making it necessary to obtain cartographic information in order to study its stability status and carry out the technical project to determine the necessary works to be done on the damaged cut-slope. Traditional techniques (GNSSs, terrestrial laser station, total station, etc.) were not possible to use here because of the terrain morphology.

3. Materials and methods

The workflow of this section is summarized in Fig. 3.

3.1. Image collection

A rotary-wing UAV with eight rotors and MikroKopter (Moormerland, Germany) electronic boards was used to collect the images. It has a payload of 2.5 kg, and the sensor was mounted to a motion-compensated gimbal. The sensor was a Nikon 3100 reflex camera with a 16 mm fixed focal length lens. This camera has a complementary metal-oxide semiconductor (CMOS) sensor of 14.8 effective megapixels with a size of 355.7 mm^2 (23.1 × 15.4 mm). Fig. 4 shows the entire system.

The flight plan was programmed and loaded into the UAV using the MikroKopter-Tool software. Two flights were executed varying the photography axis: one with a horizontal orientation and one with the axis tilted 45° downwards. Fig. 5 shows the flight lines defined by the UAV in every flight plan. During these flights, the UAV remained in a vertical plane at a distance of approximately 50 m from the studied surface. The flight plan with a horizontal photography axis consisted of four passes 150 m in length at different altitudes (20, 50, 80 and 110 m). The overlap between pictures was 90% in the vertical flight direction and 60% in the horizontal flight direction. A total of 72 images were selected to be processed in the photogrammetric procedure. The flight plan with a tilted photography axis consisted of two passes 150 m in length at altitudes of 50 and 110 m. A total of 36 images were selected to be processed in the photogrammetric projects. As the image resolution was adjusted to 4240 × 2832 pixels, the ground sample distance (GSD) was 1.86 cm. Furthermore, the 3D coordinates of 26 points scattered on the studied surface were measured with a total station without a reflector.

In this work, the coordinates of 18 points located on the cut-slope were measured with the total station. It was very difficult to locate points on the cut-slope which could be identified in the photos to georeference the point cloud. Vertices of characteristic shapes or metallic pieces of previous works on the cut-slope were used. The altitude of these points could not be greater than around 35 m from the road level because the angle of the total station telescope became very high, making it impossible to look through the telescope. Furthermore, the coordinates of eight points scattered on the road and marked with targets of A4-format size (210 × 297 mm) were measured with the total station and with GNSS to refer the coordinate system of the total station to the ETRS89 system.

The GNSS measurements were made by working with differential corrections in real-time kinematic (RTK) mode, with the base station on a geodesic pillar located within 1 km from the studied site. Both the rover and base GNSS receivers were Trimble R6 units. With this configuration, the maximum horizontal and vertical RMSs were ± 9 and ± 16 mm, respectively. The total station used was a Stonex STS22R model, which has an accuracy of 5 mm + 2 ppm in reflector-less fine mode.

3.2. Image processing

The images were processed using the software Pix4Dmapper Pro, version 3.1, which incorporates the SfM procedure described in [42] and has a three-step workflow. The results of the first step are the internal camera calibration parameters, the relative camera position and orientation corresponding to each picture, and the 3D relative coordinates of a sparse point cloud of the terrain. The second step achieves a densification of the point cloud, and a more detailed 3D model than that of step 1 is obtained. Furthermore, as the images taken in this work were not geotagged, the point cloud was georeferenced using the coordinates of the measured GCPs and CPs. Finally, in the third step, a grid DSM can be generated at a specific grid size and the orthophoto is exported at a pre-selected resolution. The bundle adjustment can be carried out using only three GCPs, but it is advisable to use more than three to obtain optimal accuracy [38,39,43,44]. Five measured points were used as GCPs and the other 18 points as CPs.

In order to evaluate the influence of the photography axis orientation on the point cloud and orthophoto accuracies, three different photogrammetric projects were considered: one using the 72 images taken with horizontal axis orientation, one using the 36 images taken with the axis tilted 45°, and one combining all 108 images (horizontal and tilted axis).

As the studied surface is almost vertical, the orthophoto obtained when projecting on a horizontal plane does not offer valuable information and even offer confusing information, because there are zones where, for a given X and Y coordinate, two or more Z coordinates can be present. To avoid this circumstance, a plane was adjusted to the cut slope surface and used for projection in order to build the orthophoto. This plane was determined by fitting the terrain point cloud obtained in the second step of the image processing previously described. For this task, only the points centred on the area of interest were taken into account. This method is similar to that of terrestrial photogrammetry or close-range photogrammetry when studying, for

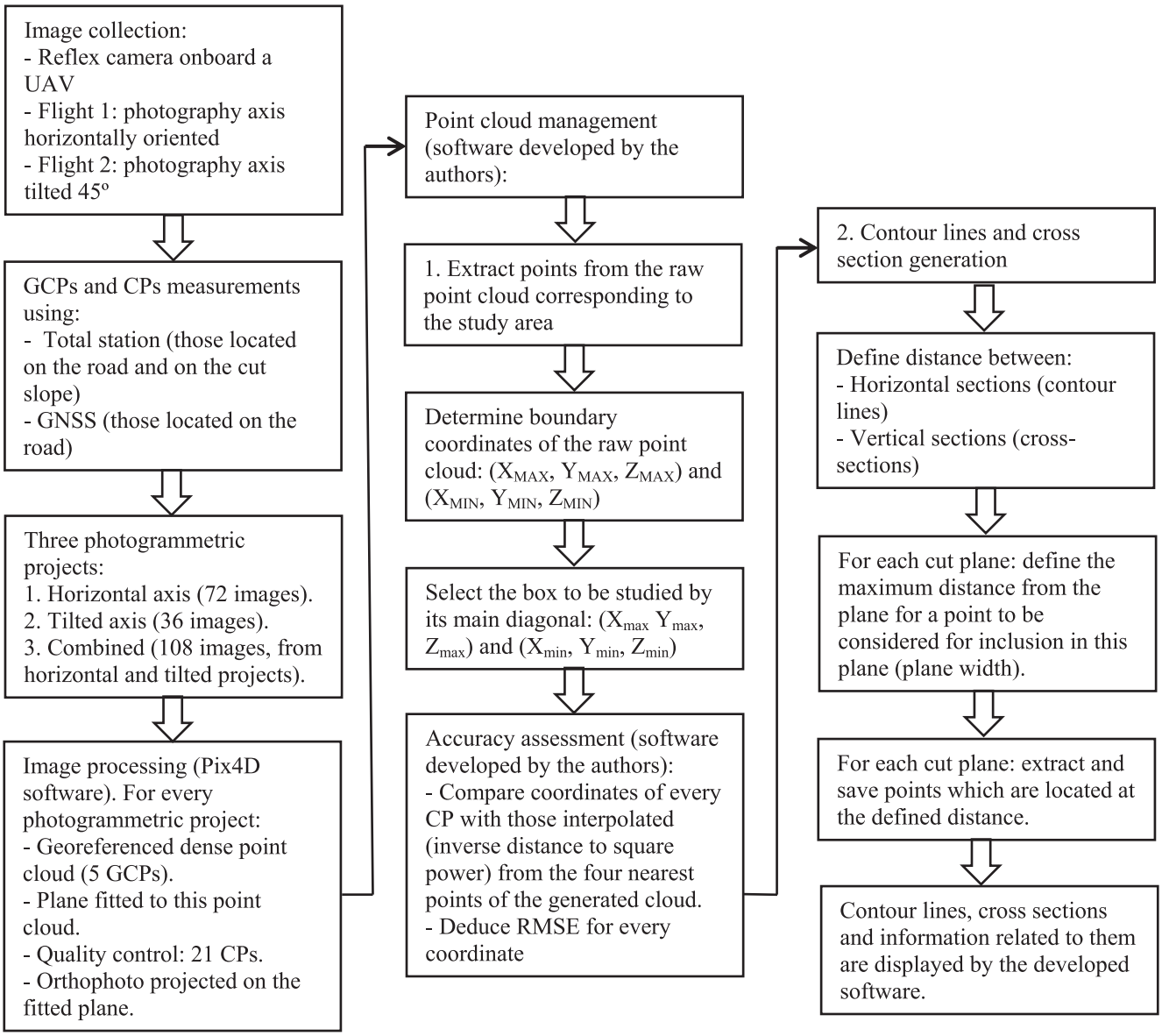

Fig. 3. Flow diagram of processing steps described in Section 3.

example, facades, but it is not common in civil engineering when working with topographic surfaces.

3.3. Point cloud management

Coordinates of the dense point cloud obtained from the photogrammetric process were referred to as UTM Zone 30N (ETRS89) and the elevation at mean sea level using the EGM08 geoid model. Standard programs that can generate a DSM from a point cloud only give one Z coordinate for each planimetric point (X, Y). So, terrains with morphology similar to the one studied in this work are incorrectly represented. In addition, there are no commercial software packages in which, clicking on a point in the orthophoto, the contour line and the cross-section corresponding to this point are generated, essential

Fig. 4. UAV equipment used in this work.

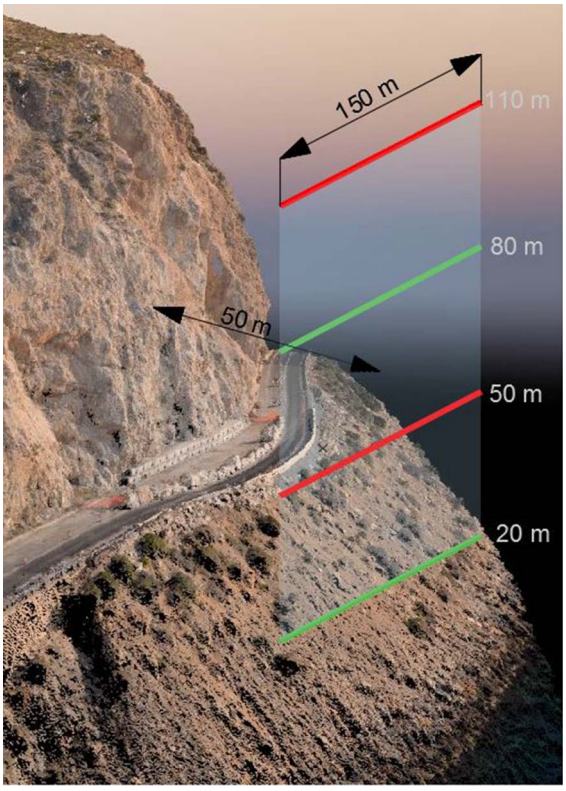

Fig. 5. Flight lines defined by the UAV in every flight plan. Red lines represent flight plan with 45° tilted photography axis. Red and green lines represent flight plan with horizontal photography axis. All flight lines had a length of 150 m and all were included in a vertical plane separated 50 m from the terrain. (For interpretation of the references to colour in this figure legend, the reader is referred to the web version of this article.)

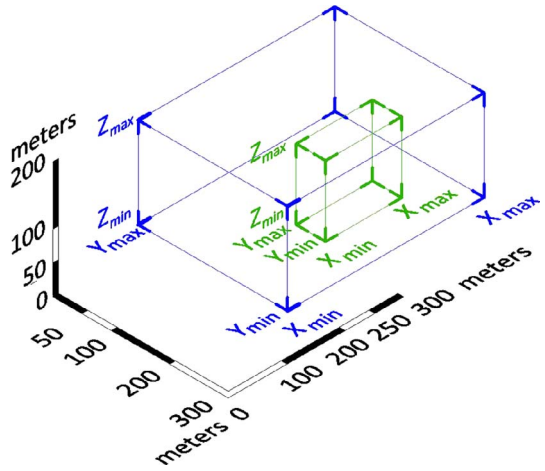

Fig. 6. Selection of the box delimiting the work area using the software developed in this study. Blue prism indicates the whole space covered by the pictures and the green prism indicates the selected study area. (For interpretation of the references to colour in this figure legend, the reader is referred to the web version of this article.)

information for the development of any engineering project related to the terrain. Therefore, to obtain the most out of the information provided by the point cloud, a software program was developed by the authors, using the Visual Basic 6.0 programming language, to obtain contour lines and cross-sections from the raw point cloud produced by vertical planes and planes perpendicular to the fitted plane at any point of the work area. This kind of terrain representation produces a very realistic visualization of the surface shape and is useful to plan and execute works on the terrain under study. The software program developed has two main parts. In the first part, contour lines and vertical

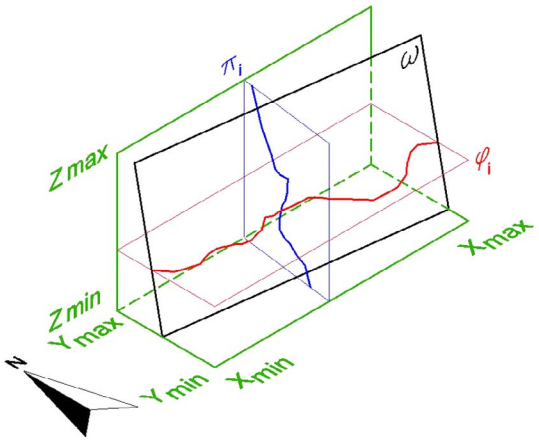

Fig. 7. Horizontal (contours level, red line) and vertical (cross-section, blue line) sections determined by cut–planes using the software developed in this study. ω represents the fitted plane that has been fit to the point cloud; ϕ_i is a generic horizontal cut-plane, which generates a contour line; and π_i is a generic vertical cut-plane, which generate a cross-section. (For interpretation of the references to colour in this figure legend, the reader is referred to the web version of this article.)

sections are extracted from the point cloud. First, from the raw point cloud generated in the photogrammetric project, which is included in the box defined by (X_{MAX}, Y_{MAX}, Z_{MAX}) and (X_{MIN}, Y_{MIN}, Z_{MIN}) (blue box in Fig. 6), a reduced box strictly centered on the study site can be defined by (X_{max}, Y_{max}, Z_{max},) and (X_{min}, Y_{min}, Z_{min}) (green box in Fig. 6). Second, contour lines and cross-sections are generated (red and blue lines, respectively, in the Fig. 7. In this figure, ω represents the fitted plane that has been fit to the point cloud; ϕ_i is a generic horizontal cut-plane, which generates a contour line; and π_i is a generic vertical cut-plane, which generate a cross-section. Furthermore, the width of the vertical and horizontal cut-planes (ϕ_i and π_i) can be adjusted in order to include a large enough number of points in the corresponding section. This is a critical adjustment because the accuracy of the sections depends on this value. If it is too low, few points will be extracted and the section will be poorly defined. On the other hand, if this value is too high, a large number of points will be extracted and the section will be defined with confusing results. Thus, to obtain an optimal value, a software program was developed to compare the results, taking into account several values for the cutting plane width.

The second part of the program developed involves displaying the generated sections. Its interface shows three graphical windows (Fig. 8): the main window for the orthophoto, projected on the fitted plane; second one for the contour line, above the orthophoto window; and a third for the cross-section. When a click is performed on the cut-slope image, a cross appears at that location, representing the intersection of the horizontal (red) and vertical (blue) planes with the terrain and, immediately, the contour line and the cross section are drawn in their respective windows. Boundary coordinates of each window and contour line elevations are shown. Furthermore, when the cursor is on the orthophoto, the terrain coordinates are displayed at the bottom.

3.4. Accuracy assessment

For every CP, the assessment of accuracy in easting (X), northing (Y), and height (Z) was performed by comparing the CP-measured coordinates with the interpolated coordinates from the four nearest points of the dense cloud generated by the photogrammetric process, resulting in $RMSE_X$, $RMSE_Y$, and RMS_{EZ} accuracy measures, respectively:

$$RMSE_X = \sqrt{\frac{\sum_{i=1}^{n} (X_{si} - X_{ci})^2}{n}} \quad (1)$$

Fig. 8. Interface of the software program developed to draw contour levels and vertical sections from the point cloud. The red straight line represents the horizontal plane and the blue straight line represents the vertical plane cutting the point cloud. The contour line is represented in the top window by red dots and the cross-section is represented in the right window by blue dots. (For interpretation of the references to colour in this figure legend, the reader is referred to the web version of this article.)

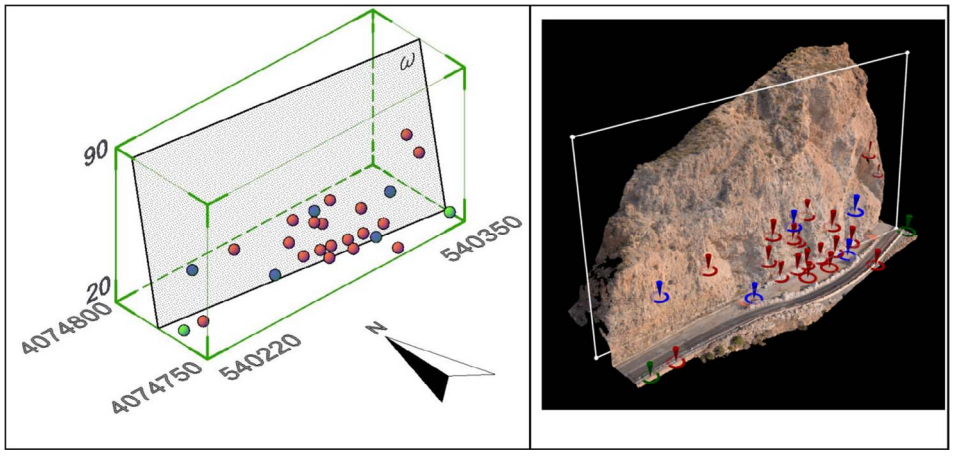

Fig. 9. Schematic (left) and realistic (right) representation of the spatial distribution of the measured points as GCPs (blue and green dots), CPs (red dots), and points for orientating the total station measurements (green dots). ω represents the plane that has been fit to the point cloud. (For interpretation of the references to colour in this figure legend, the reader is referred to the web version of this article.)

$$RMSE_Y = \sqrt{\frac{\sum_{i=1}^{n}(Y_{si}-Y_{ci})^2}{n}} \quad (2)$$

$$RMSE_Z = \sqrt{\frac{\sum_{i=1}^{n}(Z_{si}-Z_{ci})^2}{n}} \quad (3)$$

where:

n: number of CPs.
X_{si}, Y_{si}, and Z_{si}: X, Y, and Z coordinates measured with the total station for the ith CP.
X_{ci}, Y_{ci}, and Z_{ci}: X, Y, and Z coordinates of the interpolated point from the cloud.

The interpolation method chosen was the inverse distance to square power. A software program was developed in Visual Basic V6.0 for carrying out this task.

4. Results

Boundary coordinates of the box containing the raw point cloud were (540,117, 4,074,712, 0) and (540,453, 4,074,967, 143), corresponding to dimensions of 336 × 255 × 143 m. As the area of interest

Table 1
Coordinates of the measured points (Xm, Ym, Zm), error in X, Y and Z directions (E_X, E_Y, E_Z) for each photogrammetric project derived from horizontal photography axis (horizontal), 45° tilted axis (45° tilted), and combined project (combined), error range of variation (maximum error minus minimum error), average error and RMSE of the X, Y, and Z directions and photogrammetric projects. All coordinates are referred to UTM Zone 30N (ETRS89) and the elevation at mean sea level using the EGM08 geoid model. [1] indicates the points used as GCPs. The rest of the points were used as CP. [2] indicates points used for orienting the total station measurements.

Id.	Measured coordinates			Combined			Horizontal			45° tilted		
	X_m	Y_m	Z_m	E_x	E_y	E_z	E_x	E_y	E_z	E_x	E_y	E_z
1[1]	540239.58	4074779.392	35.811									
2	540259.982	4074778.526	35.746	0.02	0.09	0.01	0.04	0.10	0.06	0.06	0.12	0.12
3	540287.114	4074769.942	24.147	0.07	−0.02	0.05	0.08	−0.06	0.10	0.10	−0.06	0.09
4	540294.329	4074768.602	24.180	−0.03	−0.06	−0.01	−0.05	−0.09	−0.15	−0.70	−0.08	−0.05
5	540299.056	4074767.729	24.244	0.03	−0.04	0.02	0.06	−0.10	0.12	0.05	0.05	0.08
6	540306.281	4074766.394	24.280	0.01	−0.03	0.03	0.04	−0.06	0.06	0.03	0.05	0.10
7	540313.089	4074765.387	24.334	0.02	−0.07	−0.02	0.05	−0.11	0.06	0.06	−0.10	−0.08
8	540322.771	4074764.752	24.454	0.08	−0.04	0.01	0.10	−0.08	0.12	0.12	−0.09	0.09
9[1]	540329.708	4074768.652	33.587									
10	540315.718	4074769.421	32.360	0.02	−0.10	−0.02	0.06	−0.09	0.09	0.05	−0.10	−0.08
11	540298.763	4074772.219	32.008	−0.03	−0.13	−0.06	−0.07	−0.02	−0.09	−0.06	−0.15	−0.10
12	540281.862	4074772.198	31.625	−0.01	0.04	0.09	−0.04	0.09	−0.03	−0.03	0.07	0.12
13	540284.104	4074772.528	40.590	−0.07	−0.05	0.02	−0.09	−0.08	−0.11	−0.09	−0.09	0.08
14[1]	540293.545	4074771.006	40.984									
15	540293.42	4074770.882	35.962	−0.03	−0.11	0.03	−0.07	−0.12	−0.10	−0.08	−0.16	0.08
16	540302.084	4074771.639	41.437	−0.04	−0.10	0.06	−0.05	−0.12	−0.07	−0.07	−0.12	0.09
17	540345.107	4074769.425	43.532	−0.05	0.04	−0.02	−0.08	0.08	0.13	0.10	0.08	−0.05
18	540341.672	4074772.535	51.677	−0.05	−0.08	−0.09	−0.09	−0.09	0.10	0.08	−0.10	−0.10
19[1]	540272.788	4074770.053	22.426									
20	540294.803	4074764.157	22.753	0.08	0.04	−0.10	0.10	0.07	−0.09	−0.07	0.10	−0.15
21	540305.133	4074762.18	22.874	−0.07	0.04	−0.09	−0.09	0.07	0.09	0.06	0.06	−0.09
22[1]	540316.384	4074761.928	22.914									
23[2]	540346.656	4074754.387	23.533	−0.05	−0.06	−0.07	−0.10	−0.07	−0.09	−0.07	−0.09	−0.08
24	540317.141	4074750.767	23.444	0.02	0.10	0.12	0.05	0.15	0.05	0.03	0.12	0.15
25	540234.241	4074767.622	21.255	−0.09	0.06	−0.05	−0.11	0.14	−0.08	−0.05	0.10	−0.16
26[2]	540225.189	4074768.419	21.047	0.08	0.03	0.09	0.09	0.05	0.13	0.09	0.08	0.10
			Range	0.170	0.230	0.218	0.210	0.270	0.280	0.275	0.280	0.310
			Average	−0.004	−0.020	0.000	−0.008	−0.017	0.003	0.014	−0.015	0.008
			RMSE	**0.053**	**0.070**	**0.061**	**0.075**	**0.090**	**0.080**	**0.093**	**0.100**	**0.101**

was smaller than the total covered area, this was reduced using the software program described in Section 3 (Figs. 6 and 7). The boundary coordinates of the study area were (X_{min} = 540,220, Y_{min} = 4,074,750, Z_{min} = 20) and (X_{max} = 540,350, Y_{max} = 4,074,800, Z_{max} = 90), corresponding to dimensions of 130 × 50 × 70 m. Taking into account this reduced box, the number of points in the generated clouds were 2,640,231 for the horizontal axis project, 220,192 for the 45° tilted project, and 2,933,590 for the combined project. In this way, all tasks carried out on the point cloud were completed in a much shorter time due to the smaller number of points to be handled.

Fig. 9 shows a schematic (left) and realistic (right) representation of the CPs (red dots) and GCPs spatial distribution (blue dots). In this figure the two green dots are the points used for the orientation points measured with the total station, and ω represents the plane that was fit to the point cloud of the corresponding photogrammetric project and, which was used as the projection plane to make the orthophoto.

Table 1 shows the 3D coordinates of the 18 points measured on the cut-slope and the eight measured on the road (columns X_m, Y_m, and Z_m). Points 1, 9, 14, 19, and 22 were used as GCPs and the rest were used as CPs. Furthermore, points 23 and 26 were used for orienting the coordinates measured with the total station.

In Table 1 and Fig. 9 it can be observed that the maximum altitude of the measured points was 51.677 m. It was not possible to measure points located at higher altitudes due to the limitations explained in Section 3. Furthermore, Table 1 shows the errors for the X, Y and Z coordinates of every CP for each photogrammetric project (horizontal axis, tilted axis and combined) taking into account the measured coordinates and estimated coordinates from the point cloud as described in the Accuracy assessment section as well as the range of variation of the error (maximum error minus minimum error), the average error, and the RMSE of the X, Y, and Z directions. For the three components, the lowest variation in error ranges was found in the combined project and the highest in the tilted project. If the projects are studied separately, the variation of the error ranges for the three coordinates were similar. The RMSE for the X, Y, and Z directions were 0.053 m, 0.070 m and 0.061 m respectively for the combined project; 0.075 m, 0.090 m, and 0.079 m for the horizontal photography axis project; and 0.093 m, 0.097 m and 0.101 m for the tilted photography axis project. So, the best accuracy was achieved by the combined project, which included horizontal and tilted images. From here on, all results discussed refer to the combined project.

Fig. 10 shows the orthophoto obtained using a horizontal plane (a) and that obtained using the fitted plane (b). GSD was 1.86 cm, which represents a very good spatial resolution for inspections and stability studies. Each of these two images gives complementary information, but if they are to be used to repair the cut-slope, orthophoto (b) will be more useful than (a).

As stated in the Point Cloud Management section, a critical adjustment of the software program developed was to select the cutting plane width for generating contour lines and cross-sections. Extraction of intersection points between the point cloud and the cutting plane was carried out using plane widths of 0.5 cm, 1 cm, 2 cm, and 5 cm and by comparing the results using the developed software program for this purpose, mentioned in the Point Cloud Management section. Fig. 11 shows the results for three different cross-sections (CS1, CS2, and CS3). The axes have not been graduated because the purpose of this figure is to compare the same section with different numbers of points. The number at the bottom of each section is the number of points extracted from the point cloud. When a width of 0.5 cm is selected, the observed accuracy of the cross-section representation is not sufficient (103 points for CS1, 129 for CS2, and 141 CS3) because gaps exist between the extracted points. When a width of 5 cm is selected, representative sections are constructed with a large number of extracted points (1140 for CS1, 1232 for CS2, and 1288 CS3) and the section is not clearly defined.

Fig. 10. Orthophotos obtained using a horizontal projection plane (a), and using the plane that has been fit to the point cloud generated during the photogrammetric process (b).

Nevertheless, differences between sections using widths of 1 cm (219 for CS1, 259 for CS2, and 276 CS3) and 2 cm (434 for CS1, 499 for CS2, and 561 CS3) were not remarkable, and both values yielded well-defined representative sections. For our study, the 1 cm width was chosen to generate the contour lines and cross-sections.

Fig. 12 shows the contour lines obtained from the point cloud by standard software (a), and by the developed software (b). In the first case, no contour line crosses another, but in the second case it can be observed that several contour lines cross other lines.

Fig. 13 shows several cross-sections in which it can be observed that for a given planimetric point (X, Y), there may be more than one value for Z because the terrain morphology can be properly represented if these sections are generated from the point cloud by the developed software (blue lines in Fig. 13). This would not have been possible if the cross-sections had been generated from a DSM (red lines in Fig. 13).

5. Discussion

For the combined project, in which the best accuracies were found, the error of the estimated coordinates ranged from −0.085 m to 0.085 m (0.170 m) for the X component, from −0.131 m to 0.099 m (0.230 m) for the Y component, and from −0.100 m to 0.118 m (0.218 m) for the Z component, indicating similar ranges for each component. The RMSE for the X, Y, and Z directions were 0.053 m, 0.070 m, and 0.061 m, respectively. The photogrammetric projects that only used horizontal axis or tilted axis images yielded worse accuracies than those achieved by the combined project. For the horizontal axis image project, the RMSE for the X, Y and Z components were 0.075 m, 0.090 m, and 0.080 m, respectively. For the tilted axis, these values were 0.093 m, 0.100 m, and 0.101 m. So, the ranges of error and RMSE values indicate, firstly, that terrains with complex morphologies requires images taken with different axis orientation, and secondly, that results derived from the combined photogrammetric project are acceptable for the purpose of generating cartographic information for developing technical projects. Furthermore, RMSEs are similar to or better than those reported in other studies carried out under similar conditions. For instance, [31] used Agisoft PhotoScan Professional 0.85 software for the 3D terrain reconstruction and reached a geometric

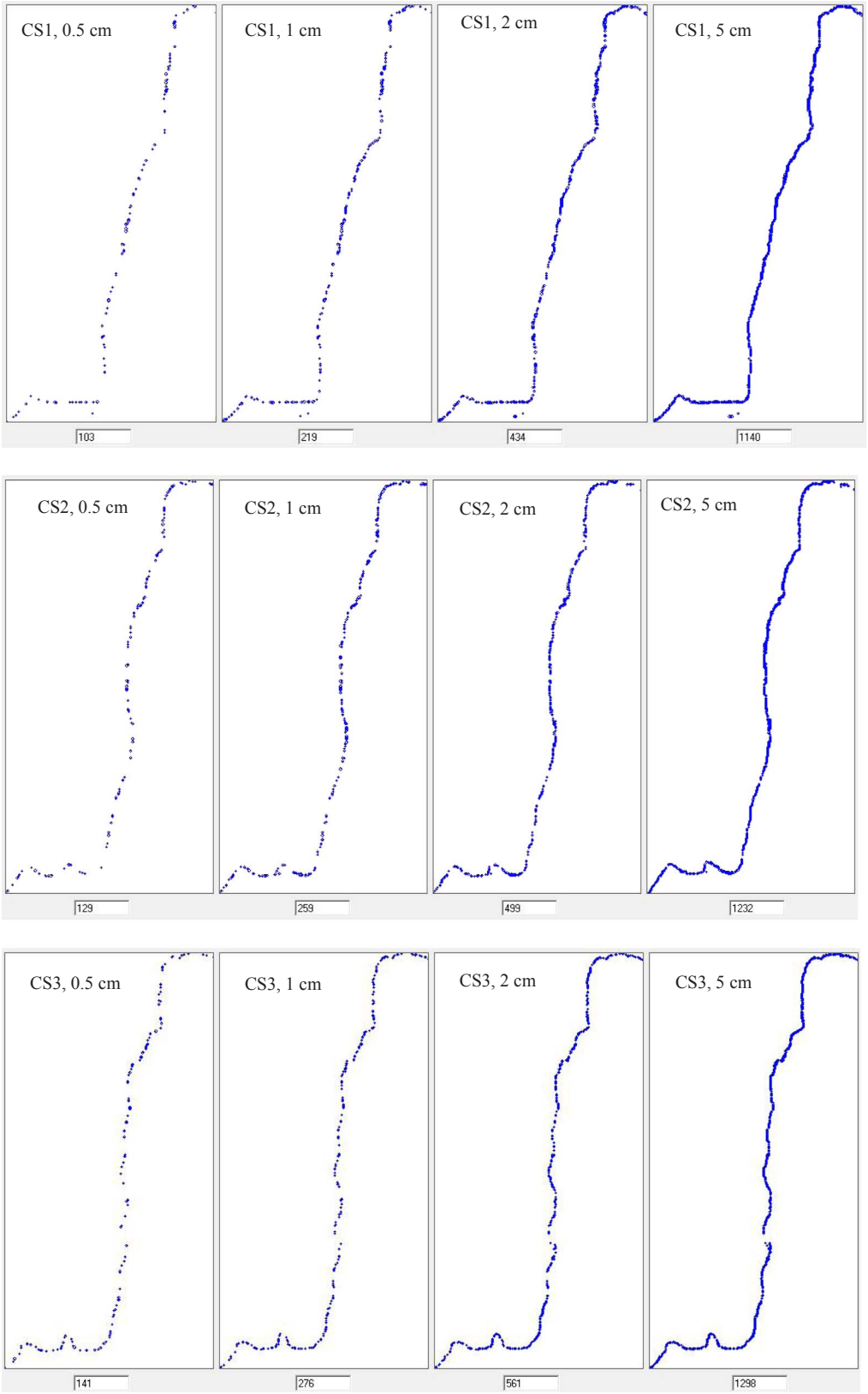

Fig. 11. Example of three cross-sections (CS1, CS2, and CS3) obtained with the software program developed in this study utilizing cutting plane widths of 0.5 cm, 1 cm, 2 cm, and 5 cm. The number at the bottom of each panel indicates the number of points included in the cross-section.

accuracy of 0.060 m in planimetry and 0.044 m in the Z component. They worked on an Antarctic surface, the flight altitude was 50 m above ground level, and the camera was similar to that used in this work. Turner et al. [45] worked under similar conditions as [31] and reported accuracies of 0.100 m for the planimetric component and 0.150 m for the Z component. Agüera-Vega et al. [38] used a UAV system similar to that used in this work to study the accuracy of digital surface models and orthophotos derived from UAV photogrammetry of terrains with

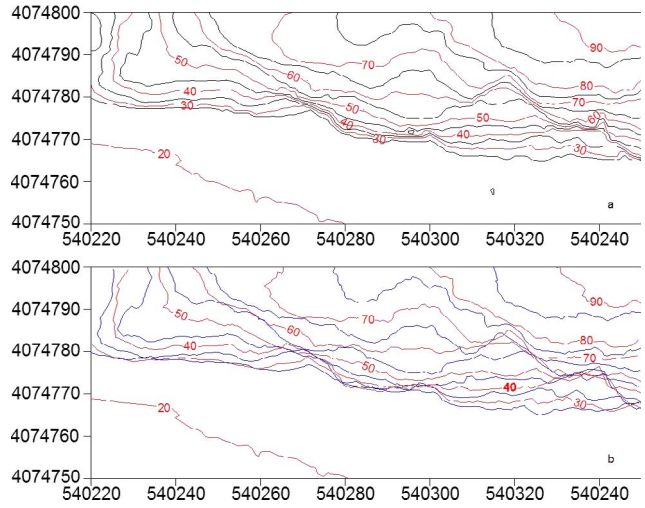

Fig. 12. Contour lines produced from the point cloud by standard software (a) and by the developed program (b). Crossing contour lines in (b) show where overhangs (negative slope areas) exist in the real terrain, which are not properly represented by the standard software.

different morphologies and compared the results for different flight altitudes and number of GCPs. At a flight altitude of 50 m and five GCPs, which are similar conditions to those of our work, they reported RMSE values around 0.050 m for the X, Y, and Z components. All these cited works used GCPs sprayed on the whole studied surface, representing better conditions than those found in our work. Hugenholtz et al. [12] reported vertical RMSE values of 0.106 m and 0.097 m derived from a photogrammetric project on a stockpile, conducted before and after a portion of the pile was removed, using a rotatory-wing UAV and flight altitude of 100 m. In complex-morphology terrains, Carvajal-Ramírez et al. [41] achieved planimetric and vertical accuracies of 0.058 m and 0.100 m, respectively, working on a road cut-slope. They used a rotatory-wing UAV and carried out two flights for the photogrammetry project, the first with the camera in the vertical position and the second with the camera oriented 45° to the terrain.

With a larger number of GCPs sprayed on the whole surface, better accuracy could likely be reached, as concluded in [46], but in terrains with very difficult morphology it is not possible to have as many points as would be desirable, even using a total station without a reflector, because there may be no representative points which can be identified in the photographs. Therefore, we cannot carry out a study of the distribution of the error across the whole surface. Even so, the accuracy achieved is very good for the purpose of generating information with the methodology described that can be used: to plan the cut-slope reparations works.

Although in civil engineering it is usual to use a horizontal plane to project the orthophoto, it is important to take into account the objective of the photogrammetric project in order to select the appropriate projection plane [47] to obtain the optimal point of view to detect, describe, and measure cracks and the location of rocks in danger of falling on the road; take measurements; or to obtain information to plan works on the terrain under study.

In Fig. 10a, parts of the cut-slope are hidden by overhangs (areas with negative slope), as can be observed near the centre of the picture. Furthermore, although the orthophoto of Fig. 10b shows the cut slope with much more detail than Fig. 10a, it does not show the road.

In addition, contour lines and cross-sections obtained from the dense point cloud give valuable information to engineers, geologists, and other technicians for proposing the necessary works on the cut-slope to repair it and avoid a new landslide. For this terrain, a DSM obtained from the point cloud by standard software would not have represented reality since, for a given set of coordinates (X, Y), a single value of the Z coordinate would be given by the DSM, but this is not the case for certain zones of the studied terrain where overhangs are present. The software program developed in this study has made it possible to obtain contour lines directly from the point cloud that faithfully represent the terrain.

6. Conclusions

The methodology proposed in this work has proven to be efficient for reconstructing very complex topography, such as a rocky cliff, in order to obtain useful information for engineers, geologists, and other technicians who are interested in the study of these types of surfaces. It is based on two flights to obtain the images to be processed in the photogrammetric project: one with the axis perpendicular to the study surface and the other one tilted 45°. In this way, better point cloud and orthophoto accuracies are reached than if only one axis orientation is considered.

The equipment used in this study, composed of a light UAV and a non-metric camera, has been shown as the only system capable of achieving that goal since, for extreme topography, terrestrial instruments, such as GNSS, terrestrial laser scanners, and aerial or space surveys, are not suitable. In this case, terrestrial instruments are useful only for the measurement of GCPs and CPs.

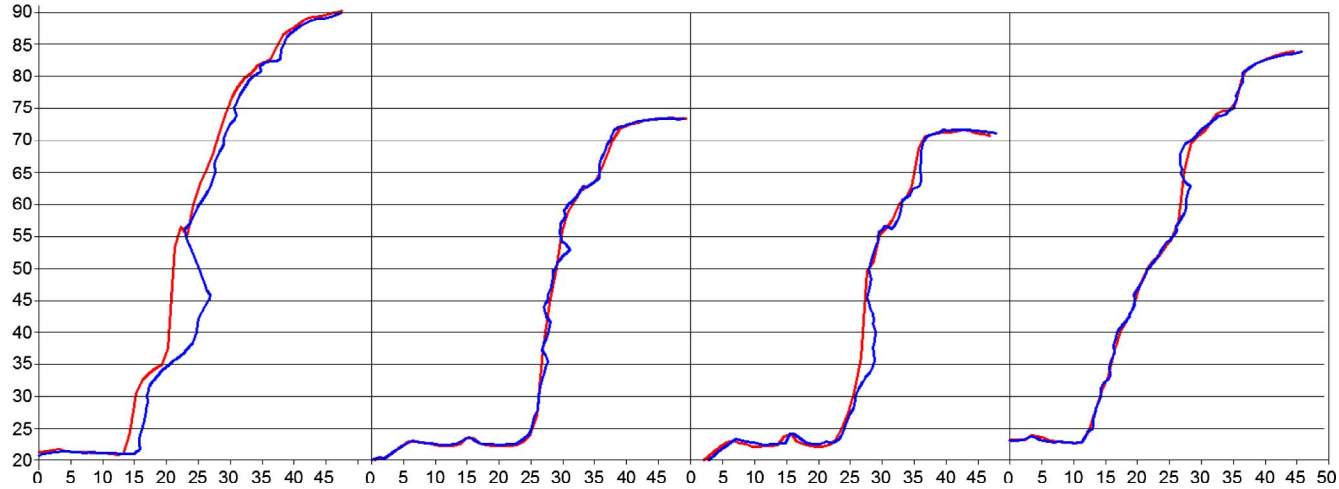

Fig. 13. Example of four cross-sections obtained from a DSM generated by a standard software (red lines), and directly from the point cloud by the developed software (blue lines). The sections obtained from the point cloud clearly represent the terrain more accurately than those obtained from the DSM. (For interpretation of the references to colour in this figure legend, the reader is referred to the web version of this article.)

For the combined project, the RMSEs found in the X, Y, and Z directions are 0.053 m, 0.070 m, and 0.061 m, respectively, similar to the best accuracies reported in other studies for similar conditions.

In addition, DSMs derived from the point cloud by standard software may not reliably represent some surfaces with very complex geometry, and it is necessary to work directly with the point cloud to generate useful information. For this purpose, the software developed in this work has proved suitable for generating manageable information, such as contour lines and cross-sections, that is useful for the development of, for example, repair or maintenance projects on cut-slopes with very complex topography. The point cloud density derived from the combined UAV photogrammetry project described in this work has allowed us to accurately represent the terrain using contour lines and cross-sections, which are the formats needed to develop plans to carry out works on the terrain. For each cutting plane that generates a contour line or cross-section, a plane width of 1 cm has been found to be sufficient for obtaining an accurate representation of these sections from the point cloud.

Further works could be focused on improvement of the proposed methodology by studying the effect of the number and distribution of GCPs, image resolution, or viewing geometry on the accuracy of the resulting cartographic products.

Acknowledgments

This work was supported by grant G-GI3000/IDIW, from Junta de Andalucía (Spain), co-financed with FEDER funds of the European Union.

References

[1] I.C. Fuller, A.R.G. Large, M.E. Charlton, G.L. Heritage, D.J. Milan, Reach-scale sediment transfers: an evaluation of two morphological budgeting approaches, Earth Surf. Process. Landforms. 28 (2003) 889–903, http://dx.doi.org/10.1002/esp.1011.
[2] J. Brasington, B.T. Rumsby, R.A. McVey, Monitoring and modelling morphological change in a braided gravel-bed river using high resolution GPS-based survey, Earth Surf. Process. Landforms 25 (2000) 973–990, http://dx.doi.org/10.1002/1096-9837(200008)25:9<973::AID-ESP111>3.0.CO;2-Y.
[3] L. Javernick, J. Brasington, B. Caruso, Modeling the topography of shallow braided rivers using Structure-from-Motion photogrammetry, Geomorphology 213 (2014) 166–182, http://dx.doi.org/10.1016/j.geomorph.2014.01.006.
[4] J. Brasington, D. Vericat, I. Rychkov, Modeling river bed morphology, roughness, and surface sedimentology using high resolution terrestrial laser scanning, Water Resour. Res. 48 (2012), http://dx.doi.org/10.1029/2012WR012223.
[5] W. Notebaert, F. Houtman, F. Van Opstal, W. Gevers, W. Fias, T. Verguts, Post-error slowing: an orienting account, Cognition 111 (2009) 275–279, http://dx.doi.org/10.1016/j.cognition.2009.02.002.
[6] R.C. Hilldale, D. Raff, Assessing the ability of airborne LiDAR to map river bathymetry, Earth Surf. Process. Landforms 33 (2008) 773–783, http://dx.doi.org/10.1002/esp.1575.
[7] S.N. Lane, The measurement of river channel morphology using digital photogrammetry, Photogramm. Rec. 16 (2000) 937–961, http://dx.doi.org/10.1111/0031-868X.00159.
[8] F. Nex, F. Remondino, UAV for 3D mapping applications: a review, Appl. Geomatics 6 (2014) 1–15, http://dx.doi.org/10.1007/s12518-013-0120-x.
[9] F. Clapuyt, V. Vanacker, K. Van Oost, Reproducibility of UAV-based earth topography reconstructions based on Structure-from-Motion algorithms, Geomorphology 260 (2016) 4–15, http://dx.doi.org/10.1016/j.geomorph.2015.05.011.
[10] A.S. Laliberte, J.E. Herrick, A. Rango, C. Winters, Acquisition, orthorectification, and object-based classification of unmanned aerial vehicle (UAV) imagery for rangeland monitoring, Photogramm. Eng. Remote Sens. 76 (2010) 661–672, http://dx.doi.org/10.14358/PERS.76.6.661.
[11] S. Harwin, A. Lucieer, Assessing the accuracy of georeferenced point clouds produced via multi-view stereopsis from unmanned aerial vehicle (UAV) imagery, Remote Sens. 4 (2012) 1573–1599, http://dx.doi.org/10.3390/rs4061573.
[12] C.H. Hugenholtz, J. Walker, O. Brown, S. Myshak, Earthwork volumetrics with an unmanned aerial vehicle and softcopy photogrammetry, J. Surv. Eng. 141 (2015) 6014003, http://dx.doi.org/10.1061/(ASCE)SU.1943-5428.0000138.
[13] J. Balek, J. Blahůt, A critical evaluation of the use of an inexpensive camera mounted on a recreational unmanned aerial vehicle as a tool for landslide research, Landslides (2016) 1–8, http://dx.doi.org/10.1007/s10346-016-0782-7.
[14] I.M. and J.B.R. James S. Aber, Small-Format Aer. Photogr. Princ. Tech. Geosci. Appl., Elsevier B.V., Amsterdam, 2010.
[15] W.W. Immerzeel, P.D.A. Kraaijenbrink, J.M. Shea, A.B. Shrestha, F. Pellicciotti, M.F.P. Bierkens, S.M. de Jong, High-resolution monitoring of Himalayan glacier dynamics using unmanned aerial vehicles, Remote Sens. Environ. 150 (2014) 93–103, http://dx.doi.org/10.1016/j.rse.2014.04.025.
[16] K. Lambers, H. Eisenbeiss, M. Sauerbier, D. Kupferschmidt, T. Gaisecker, S. Sotoodeh, T. Hanusch, Combining photogrammetry and laser scanning for the recording and modelling of the Late Intermediate Period site of Pinchango Alto, Palpa, Peru, J. Archaeol. Sci. 34 (2007) 1702–1712, http://dx.doi.org/10.1016/j.jas.2006.12.008.
[17] I. Colomina, P. Molina, Unmanned aerial systems for photogrammetry and remote sensing: a review, ISPRS J. Photogramm. Remote Sens. 92 (2014) 79–97, http://dx.doi.org/10.1016/j.isprsjprs.2014.02.013.
[18] P. Liu, A.Y. Chen, Y.-N. Huang, J.-Y. Han, J.-S. Lai, S.-C. Kang, T.-H. Wu, M.-C. Wen, M.-H. Tsai, A review of rotorcraft Unmanned Aerial Vehicle (UAV) developments and applications in civil engineering, Smart Struct. Syst. 13 (2014) 1065–1094, http://dx.doi.org/10.12989/sss.2014.13.6.1065.
[19] K.B. Atkinson, Close Range Photogrammetry and Machine Vision, Whitttles, 1996.
[20] A.Z. Richard Hartley, Multiple View Geometry, 2003. http://doi.org/10.1017/CBO9781107415324.004.
[21] N. Snavely, S.M. Seitz, R. Szeliski, Modeling the world from internet photo collections, Int. J. Comput. Vis. 80 (2008) 189–210, http://dx.doi.org/10.1007/s11263-007-0107-3.
[22] M.J. Westoby, J. Brasington, N.F. Glasser, M.J. Hambrey, J.M. Reynolds, ?Structure-from-Motion? photogrammetry: a low-cost, effective tool for geoscience applications, Geomorphology 179 (2012) 300–314, http://dx.doi.org/10.1016/j.geomorph.2012.08.021.
[23] Y. Vasuki, E.-J. Holden, P. Kovesi, S. Micklethwaite, Semi-automatic mapping of geological Structures using UAV-based photogrammetric data: an image analysis approach, Comput. Geosci. 69 (2014) 22–32, http://dx.doi.org/10.1016/j.cageo.2014.04.012.
[24] Y. Furukawa, J. Ponce, Accurate, Dense, and Robust Multi-View Stereopsis 1 (2007) 1–14. http://doi.ieeecomputersociety.org/10.1109/TPAMI.2009.161..
[25] D.G. Lowe, Object recognition from local scale-invariant features, in: Proc. Seventh IEEE Int. Conf. Comput. Vis., vol. 2, IEEE, 1999, pp. 1150–1157 http://doi.org/10.1109/ICCV.1999.790410.
[26] D.G. Lowe, Distinctive image features from scale-invariant keypoints, Int. J. Comput. Vis. 60 (2004) 91–110, http://dx.doi.org/10.1023/B:VISI.0000029664.99615.94.
[27] M. Forsman, N. Börlin, J. Holmgren, Estimation of tree stem attributes using terrestrial photogrammetry with a camera rig, Forests 7 (2016) 61, http://dx.doi.org/10.3390/f7030061.
[28] F. Remondino, S. El-Hakim, Image-based 3D modelling: a review, Photogramm. Rec. 21 (2006) 269–291, http://dx.doi.org/10.1111/j.1477-9730.2006.00383.x.
[29] L. Juan, O. Gwun, A comparison of sift, pca-sift and surf, Int. J. Image Process. 3 (2009) 143–152, http://dx.doi.org/10.1007/s11270-006-2859-8.
[30] M.A. Fonstad, J.T. Dietrich, B.C. Courville, J.L. Jensen, P.E. Carbonneau, Topographic structure from motion: a new development in photogrammetric measurement, Earth Surf. Process. Landforms 38 (2013) 421–430, http://dx.doi.org/10.1002/esp.3366.
[31] A. Lucieer, D. Turner, D.H. King, S.A. Robinson, Using an Unmanned Aerial Vehicle (UAV) to capture micro-topography of Antarctic moss beds, Int. J. Appl. Earth Obs. Geoinf. 27 (2014) 53–62, http://dx.doi.org/10.1016/j.jag.2013.05.011.
[32] F. Mancini, M. Dubbini, M. Gattelli, F. Stecchi, S. Fabbri, G. Gabbianelli, Using Unmanned Aerial Vehicles (UAV) for high-resolution reconstruction of topography: the structure from motion approach on coastal environments, Remote Sens. 5 (2013) 6880–6898, http://dx.doi.org/10.3390/rs5126880.
[33] A. Lucieer, S.M. d. Jong, D. Turner, Mapping landslide displacements using Structure from Motion (SfM) and image correlation of multi-temporal UAV photography, Prog. Phys. Geogr. 38 (2014) 97–116, http://dx.doi.org/10.1177/0309133313515293.
[34] T.N. Tonkin, N.G. Midgley, D.J. Graham, J.C. Labadz, The potential of small unmanned aircraft systems and structure-from-motion for topographic surveys: a test of emerging integrated approaches at Cwm Idwal, North Wales, Geomorphology 226 (2014) 35–43, http://dx.doi.org/10.1016/j.geomorph.2014.07.021.
[35] A. Eltner, P. Baumgart, H.G. Maas, D. Faust, Multi-temporal UAV data for automatic measurement of rill and interrill erosion on loess soil, Earth Surf. Process. Landforms 40 (2015) 741–755, http://dx.doi.org/10.1002/esp.3673.
[36] A.T. Mozas-Calvache, J.L. Pérez-García, T. Fernández-del Castillo, Monitoring of landslide displacements using UAS and control methods based on lines, Landslides (2017), http://dx.doi.org/10.1007/s10346-017-0842-7.
[37] R.M. Mateos, J.M. Azañón, F.J. Roldán, D. Notti, V. Pérez-Peña, J.P. Galve, J.L. Pérez-García, C.M. Colomo, J.M. Gómez-López, O. Montserrat, N. Devantèry, F. Lamas-Fernández, F. Fernández-Chacón, The combined use of PSInSAR and UAV photogrammetry techniques for the analysis of the kinematics of a coastal landslide affecting an urban area (SE Spain), Landslides 14 (2017) 743–754, http://dx.doi.org/10.1007/s10346-016-0723-5.
[38] F. Agüera-Vega, F. Carvajal-Ramírez, P. Martínez-Carricondo, Assessment of photogrammetric mapping accuracy based on variation ground control points number using unmanned aerial vehicle, Measurement 98 (2017) 221–227. http://doi.org/10.1016/j.measurement.2016.12.002.
[39] F. Agüera-Vega, F. Carvajal-Ramírez, P. Martínez-Carricondo, Accuracy of digital surface models and orthophotos derived from unmanned aerial vehicle photogrammetry, J. Surv. Eng. 143 (2017) 4016025. http://doi.org/10.1061/(ASCE)SU.1943-5428.0000206.
[40] T. Fernández, J. Pérez, J. Cardenal, J. Gómez, C. Colomo, J. Delgado, Analysis of landslide evolution affecting olive groves using UAV and photogrammetric techniques, Remote Sens. 8 (2016) 837, http://dx.doi.org/10.3390/rs8100837.
[41] F. Carvajal-Ramírez, F. Agüera-Vega, P.J. Martínez-Carricondo, Effects of image

orientation and ground control points distribution on unmanned aerial vehicle photogrammetry projects on a road cut slope, J. Appl. Remote Sens. 10 (2016) 34004. http://doi.org/10.1117/1.JRS.10.034004.
[42] G. Verhoeven, Taking computer vision aloft - archaeological three-dimensional reconstructions from aerial photographs with photoscan, Archaeol. Prospect. 18 (2011) 67–73, http://dx.doi.org/10.1002/arp.399.
[43] T. Rosnell, E. Honkavaara, Point cloud generation from aerial image data acquired by a quadrocopter type micro unmanned aerial vehicle and a digital still camera, Sensors 12 (2012) 453–480, http://dx.doi.org/10.3390/s120100453.
[44] K.N. Tahar, An evaluation on different number of ground control points, Int. Arch. Photogramm. Remote Sens. Spat. Inf. Sci. - ISPRS Arch. XL-2/W2 (2013) 27–29. http://doi.org/10.5194/isprsarchives-XL-2-W2-93-2013.
[45] D. Turner, A. Lucieer, C. Watson, An automated technique for generating georectified mosaics from ultra-high resolution unmanned aerial vehicle (UAV) imagery, based on structure from motion (SfM) point clouds, Remote Sens. 4 (2012) 1392–1410, http://dx.doi.org/10.3390/rs4051392.
[46] T. Tonkin, N. Midgley, Ground-control networks for image based surface reconstruction: an investigation of optimum survey designs using UAV derived imagery and structure-from-motion photogrammetry, Remote Sens. 8 (2016) 786, http://dx.doi.org/10.3390/rs8090786.
[47] Y. Li, Q. Hu, M. Wu, J. Liu, X. Wu, Extraction and simplification of building Fa?ade Pieces from mobile laser scanner point clouds for 3D street view services, ISPRS Int. J. Geo-Inform. 5 (2016) 231, http://dx.doi.org/10.3390/ijgi5120231.